HAL open science

Solar calcination at pilot scale in a continuous flow multistage horizontal fluidized bed

Thibaut Esence, Emmanuel Guillot, Michael Tessonneaud, Jean-Louis Sans, Gilles Flamant

To cite this version:

Thibaut Esence, Emmanuel Guillot, Michael Tessonneaud, Jean-Louis Sans, Gilles Flamant. Solar calcination at pilot scale in a continuous flow multistage horizontal fluidized bed. Solar Energy, 2020, 207, pp.367 - 378. 10.1016/j.solener.2020.06.098 . hal-03523228

HAL Id: hal-03523228

https://univ-perp.hal.science/hal-03523228

Submitted on 18 Jul 2022

HAL is a multi-disciplinary open access archive for the deposit and dissemination of scientific research documents, whether they are published or not. The documents may come from teaching and research institutions in France or abroad, or from public or private research centers.

L'archive ouverte pluridisciplinaire **HAL**, est destinée au dépôt et à la diffusion de documents scientifiques de niveau recherche, publiés ou non, émanant des établissements d'enseignement et de recherche français ou étrangers, des laboratoires publics ou privés.

Distributed under a Creative Commons Attribution - NonCommercial 4.0 International License

Version of Record: https://www.sciencedirect.com/science/article/pii/S0038092X2030712X
Manuscript_34ceb4bde7c0879eb581690e1d4f7106

Solar calcination at pilot scale in a continuous flow multistage horizontal fluidized bed

Thibaut Esence, Emmanuel Guillot, Michael Tessonneaud, Jean-Louis Sans, Gilles Flamant*

Processes, Materials and Solar Energy laboratory, PROMES-CNRS

7, rue du Four solaire, 66120 Font Romeu, France

*Corresponding author, gilles.flamant@promes.cnrs.fr

Abstract

Calcination of limestone for lime production was successfully performed in the continuous flow mode on a daily basis in a fluidized bed indirectly heated by concentrated solar radiation. Industrial calcium carbonate feedstock was decomposed at the focus of the CNRS 1 MW solar furnace in a pilot-scale solar reactor operating at an average power of 55 kW. The reactor was a four-stage horizontal fluidized bed, irradiated on a front metallic wall of 1 m long and 0.4 m high. A novel aiming strategy was applied to reduce the hot spots on the irradiated wall. The conversion degree was analyzed as a function of the fluidization conditions (air mass flow rate) and the particle mass flow rate. This latter parameter varied in range (14.5 – 25 kg/h), and the highest conversion degrees were obtained at high fluidization velocity. The best result was obtained for a calcite mass flow rate of 20 kg/h, resulting in a degree of conversion of 95.2%, a BET surface area of the lime of 5.39 m^2/g, and 17% and 29% thermochemical and thermal efficiencies of the reactor, respectively. This achievement corresponds to a particle mass flow rate three times higher than the current state of the art for solar calcination of lime.

Keywords

Solar calcination; fluidized bed reactor; pilot-scale continuous operation; solar thermochemistry; quicklime, solar heat in energy-intensive industry

© 2020 published by Elsevier. This manuscript is made available under the CC BY NC user license
https://creativecommons.org/licenses/by-nc/4.0/

1. Introduction

Calcination is an emblematic chemical reaction in solar thermochemistry for many reasons. First, it is a representative reaction of energy-intensive industry as well as lime and cement production, which is responsible for approximately 7-8% of worldwide anthropogenic CO_2 emissions (Olivier et al., 2016). Second, calcination occurs at 800-900 °C, a temperature level that corresponds to the optimum operation temperature of point-focusing systems with a mean concentration of 1000 (Fletcher and Moen, 1977; Li et al., 2016). Third, calcination is a solid-gas reaction that necessitates the processing of specific reactor developments with solar energy.

In the lime industry, limestone is processed to produce lime in two main reactor types, shaft kilns and rotary kilns (EuLA, 2020). Shaft kilns are vertical kilns that operate in the moving packed-bed mode. The limestone being processed is fed from a top hopper in a vertical chamber in which the static bed moves downward in plug flow. The particle diameters range from 20 mm to 175 mm. Twin shaft parallel flow regenerative kilns are composed of two interconnected shafts fired in sequence to achieve excellent energy efficiency; the particle diameters are usually between 90 mm and 125 mm. Rotary kilns are rotating cylinders inclined at an angle of 3 to 4 degrees horizontally. They process particle sizes in the 15 – 40 mm range. They are fueled by coal, petroleum coke, natural gas, and waste-derived fuels. In contrast, twin shaft kilns that produce high-purity and high-reactivity quicklime are fueled with natural gas. Single-chamber shaft kilns can be operated on natural gas as well as liquid and solid fuels. Fluidized beds are marginally used in the lime industry for highly reactive products.

In traditional processes, the heat of reaction is supplied by combustion of carbon-based fuels. Under these conditions, approximately 40% of the total CO_2 emissions from lime production are related to combustion; the rest is due to chemical reaction. Consequently, replacing fossil combustion with renewable energy in limestone calcination can result in 40% reduction of CO_2 emissions. One possible option is using biomass, either solid or gas, as a heat source. The main advantage of this choice is the ability to operate existing kilns in continuous mode using this fuel. Nevertheless, burning biomass prevents the increase of this feedstock's value with the synthesis of carbon-based chemicals and fuels. Moreover, solid biomass contains minerals (Na, K, Si, P…) that can pollute the lime. Concentrated solar energy can provide high temperatures without producing any additional byproducts, thereby offering a renewable option for the production of high-quality lime.

The development of solar calcination started more than forty years ago with the demonstration of batch calcium carbonate decomposition in lab-scale solar fluidized beds and rotary kilns (Flamant et al. 1980). However, the development of solar fluidized-bed reactors (Tregambi et al., 2018) never achieved both continuous operation and pilot scale. Vortex-type reactors, such

as cyclones, have been developed to process small particles (diameter typically less than 10 µm) in continuous-flow solar reactors (Imhof, 2000, 1997; Nikulshina et al., 2009; Steinfield et al., 1991). Solar rotary kilns were demonstrated at the power level of approximately 10-15 kW in both indirect-heating configurations (Meier et al., 2006) and direct-heating configurations (Moumin et al., 2019). Meier et al. (2006) processed 1–5 mm limestone particles in an indirectly heated 10 kW_{th} multitube rotary kiln prototype. The best result reflected a lime production of 3.85 kg/h (6.88 kg/h limestone) with a conversion degree of 98% and a thermochemical efficiency of 34.8%; the maximum measurement uncertainty was estimated as ± 15.2%. This previous research addressed large particles (mean diameter larger than 1 mm). In contrast, the recent developments of Moumin et al. (2019) dealt with the calcination of fine cohesive particles in a rotary kiln. They performed the calcination of cement raw meal (particle-size distribution in the range of 1–176 µm, with 50% smaller than 15 µm) with a conversion degree of up to 99%. This latter value was achieved for a 4 kg/h feedstock mass flow rate, corresponding to a thermochemical efficiency and an overall efficiency of approximately 10 and 20%, respectively.

Esence et al. (2020) demonstrated the concept of a solar horizontal fluidized bed for the first time at lab scale for the continuous calcination of dolomite. The half decomposition of a continuous stream of 9.4 kg/h dolomite ($CaMg(CO_3)_2 \rightarrow CaCO_3 + MgO + CO_2$) was performed with a conversion degree of 100%. The measured thermochemical efficiency was 6.6%.

Accounting for the previous state of the art, this paper presents the development of solar horizontal fluidized bed technology at pilot scale (45-65 kW_{th}) for the continuous processing of limestone, which has never been demonstrated in a solar fluidized bed to date. The other objective of the work was to demonstrate solar calcination of limestone with a mass flow rate greater than 10 kg/h. The solar reactor and the aiming strategy are presented in the next section. Then, the experimental results are examined with a detailed analysis of the influence of process parameters on the conversion degree. Finally, the product quality and the reactor performance are analyzed.

2. Experiment

The complete experimental setup was implemented at the focus of the CNRS 1 MW-solar furnace. It was composed of a cavity reactor, a particle-feeding device, a particle sampling system, and an exhaust gas treatment, including a CO_2 analyzer and pressurized air distribution system, as illustrated in Figure 1.

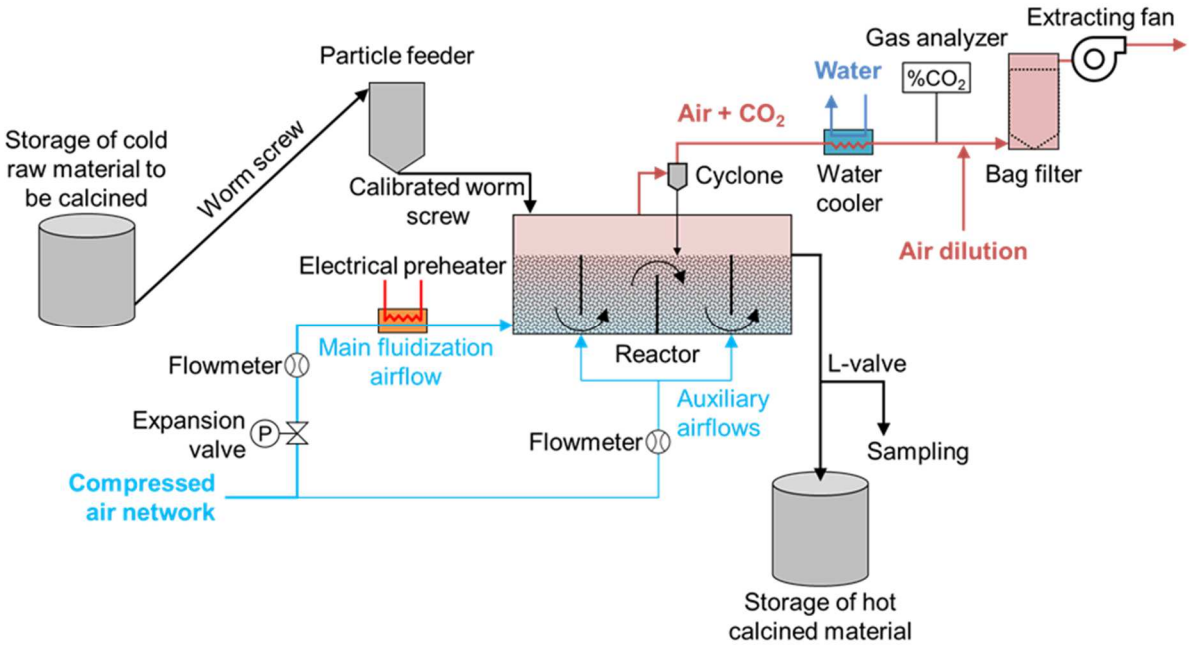

Figure 1. Schematic of the complete experimental continuous calcination setup installed at the focus of the 1-MW CNRS solar furnace.

The next sections describe the main components of the experimental setup.

Solar receiver-reactor

The solar receiver-reactor was composed of the reactor itself acting as a solar absorber and the cavity where it was located. The key component was the fluidized-bed reactor depicted in Figure 2. The reactor was a multistage horizontal fluidized bed manufactured by COMESSA.

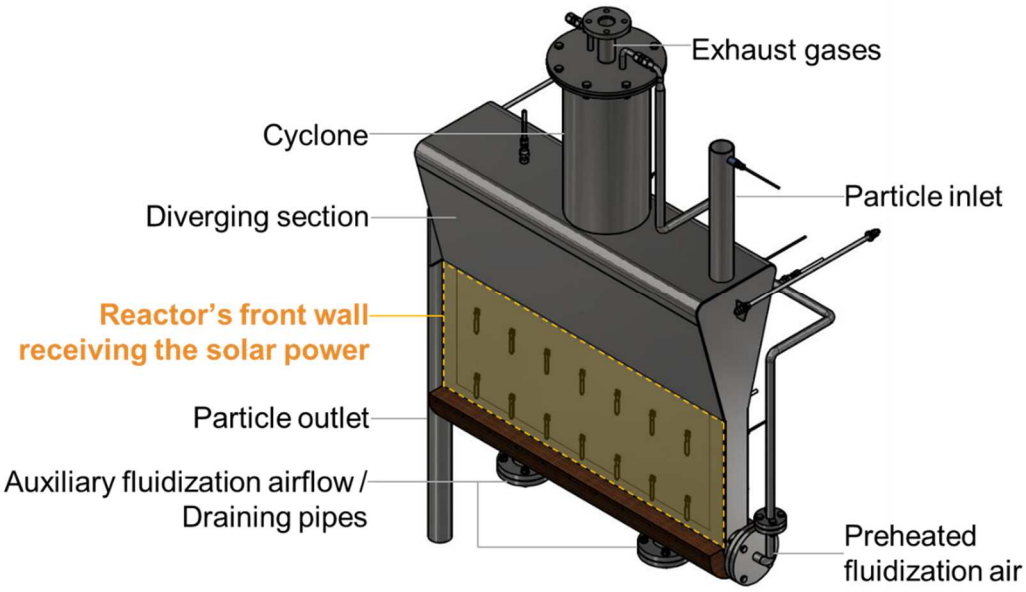

Figure 2. The pilot-scale solar reactor.

The reactor was built in Incoloy® 800HT (nickel 32%, chromium 20%, iron 48%) that can sustain temperatures up to 1100 °C. It was 1-m long and had an internal width of 8 cm. It consisted of four 25 cm-long compartments in series in which the fluidized particles were heated with solar energy to carry out the calcination reaction.

During operation, the front wall was irradiated and heated by concentrated solar flux. The heat absorbed by the front wall was transferred to the fluidized particles circulating in the reactor by conduction, convection and radiation. The concentrated solar energy provided the sensible heat and the reaction enthalpy required to perform the endothermic calcination reaction. The front wall of the reactor was initially coated with high-temperature paint, Pyromark® 2500, in order to improve its optical properties (increase the solar absorptivity and decrease the infrared emissivity). After several hours of operation, the paint was degraded by the concentrated solar flux and was naturally replaced by metallic oxides (especially chromium oxide) produced by the accelerated aging of the reactor. This was not an issue because the metallic oxides have high solar absorptivity at high temperatures, $\alpha > 0.80$ (Touloukian and Dewitt, 1970).

The particles were introduced into the first compartment of the reactor from the top. Due to fluidization, the bed of particles behaved as a fluid and overflowed by gravity from one compartment to the other until the outlet tube at the end of the fourth compartment was reached (see Fig. 3). The baffles between the compartments and the outlet of the reactor were designed so that the average height of the fluidized bed was 40 cm. This corresponded to a fluidized bed volume of 35 L, i.e., approximately 48 kg of particles (assuming a density of 2700 kg/m^3 and a void fraction of 0.5). Above the 40 cm height, a disengaging zone (conical part in Fig. 2) limited the particle entrainment. The particles leaving the reactor overflowed into the outlet tube, which was connected either to a storage tank or to a sampling vessel.

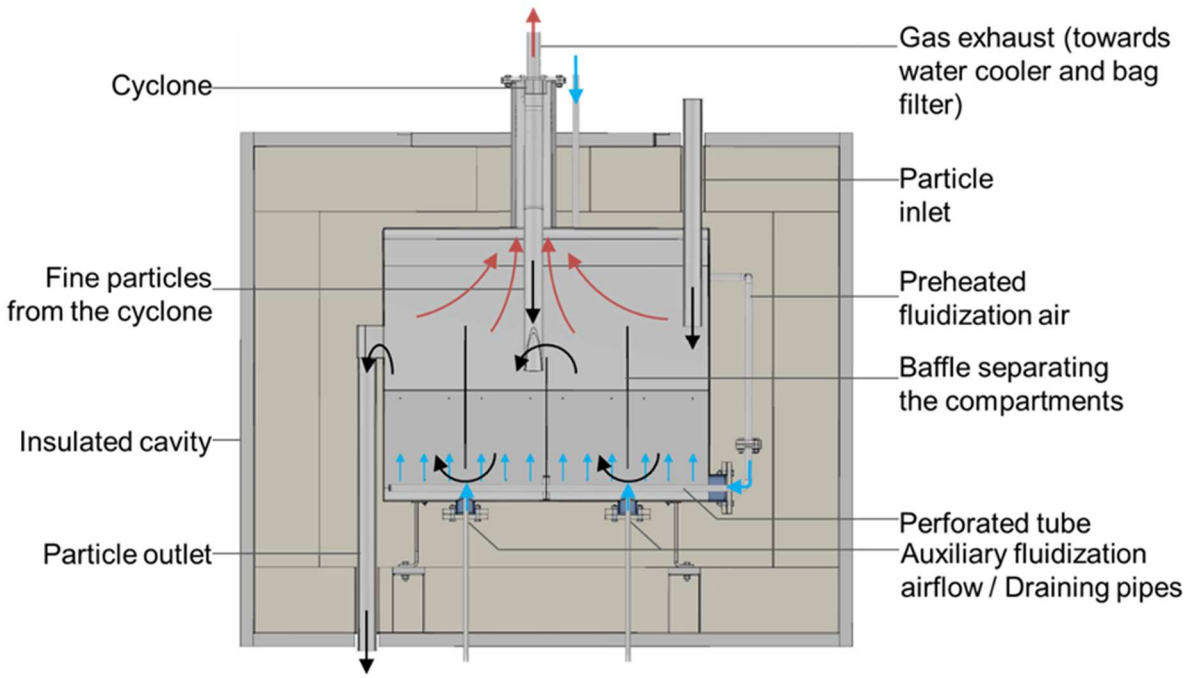

Figure 3. Cross-sectional view of the reactor-receiver inserted inside the cavity with principle of particle and gas flows (▬ particles; ▬ fluidization air; ▬ exhaust gases).

The fluidizing airflow was electrically preheated and then injected through a perforated tube located at the bottom of the reactor. In addition, two auxiliary airflows at ambient temperature were injected below the baffles of the first two and the last two compartments. These auxiliary airflows facilitated the circulation of the particles below the baffles.

The hot fluidization air and the carbon dioxide produced by the reaction were extracted at the top of the reactor. They first passed through the disengaging section, which reduced the gas velocity and hence the amount of entrained particles. The gases then passed through an internal cyclone that separated the gas and the remaining fine particles. As the fine particles fell back into the reactor, the gas (mixture of air and carbon dioxide) was extracted from the reactor.

The reactor was located in a cavity insulated with ceramic fiber (see Fig. 4-a). The cavity improved the thermal efficiency of the system by reducing the radiative and convective heat losses. A water-cooled aluminum panel protected the cavity from spilled concentrated solar energy (see Fig. 4-b). A movable water-cooled aluminum shutter matching the aperture of the cavity (80 cm x 20 cm) was placed in front of the previous panel. The shutter moved vertically to vary the size of the aperture and, as a result, to control the solar power entering the cavity. The opening of the cavity aperture was accurately measured (± 2 mm) with a ruler.

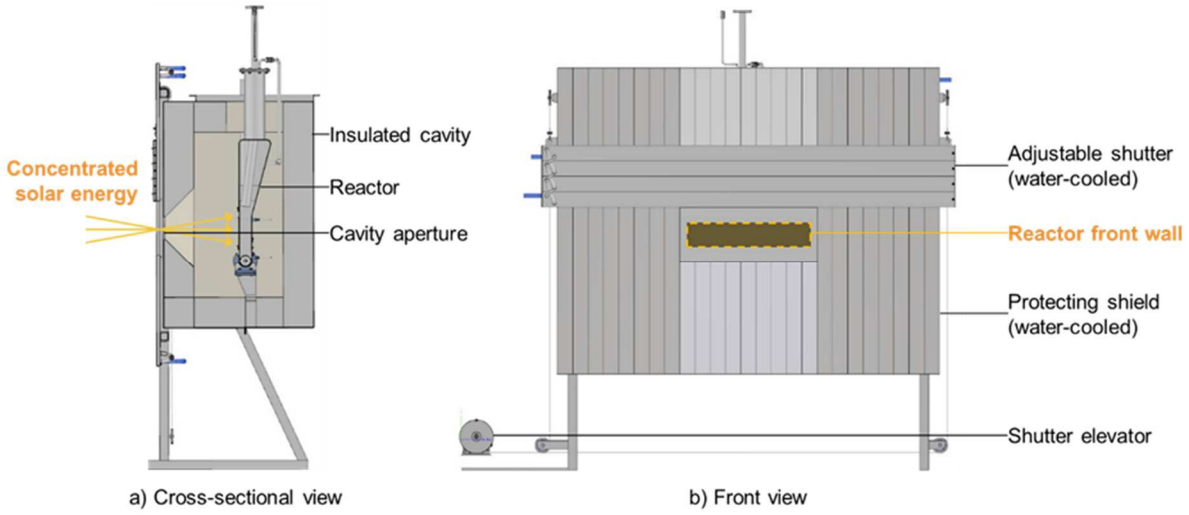

Figure 4. Schematic of the solar cavity and the protecting shield. a) Cross-sectional side view. b) Front view.

Gas and particle circuits

The particles were fluidized with air supplied by a compressor. An expander ensured that the air entered the flowmeter at 0.8 relative bar. Following the flowmeter, the airflow passed through an electrical preheater regulated to heat the air at 700 °C. Then, the airflow was injected in the reactor through the fluidization distributor (i.e., the perforated tube). Due to thermal losses between the preheater and the distributor, the temperature of the air injected in the reactor was less than 700 °C and depended on the operating conditions and temperature inside the solar cavity. Electrical heating of the fluidization air was used to hasten the heating period of the reactor and, consequently, to enable long periods of stable operation every testing day.

The CO_2 and the fluidization air drawn from the reactor and exiting from the cyclone were cooled down by a water cooler. A gas analyzer measured the CO_2 content in the extracted gases and enabled monitoring of the calcination reaction. Then, the extracted gases were diluted with an airflow that further reduced the temperature of the exhaust gases. These gases were then released into the atmosphere through a bag filter.

The particles to be calcined were stored in a large vessel (cold storage). A first worm screw periodically supplied the reactor feeder with the stored particles. The reactor feeder was equipped with a second worm screw. A variable speed motor drove the feeder's worm screw in order to control the mass flow rate of particles entering the reactor. During preliminary tests, the linear relation between the settings of the speed controller and the mass flow rate of particles was established. The particles delivered by the feeder fell on a vibrating ramp that moved the particles towards the reactor inlet. The vibrating ramp was aimed only at transporting the particles and was not intended to control the particle mass flow rate.

Instrumentation

The whole test loop was equipped with 48 K-type thermocouples. The reactor itself was equipped with 41 thermocouples (see Fig. 5).

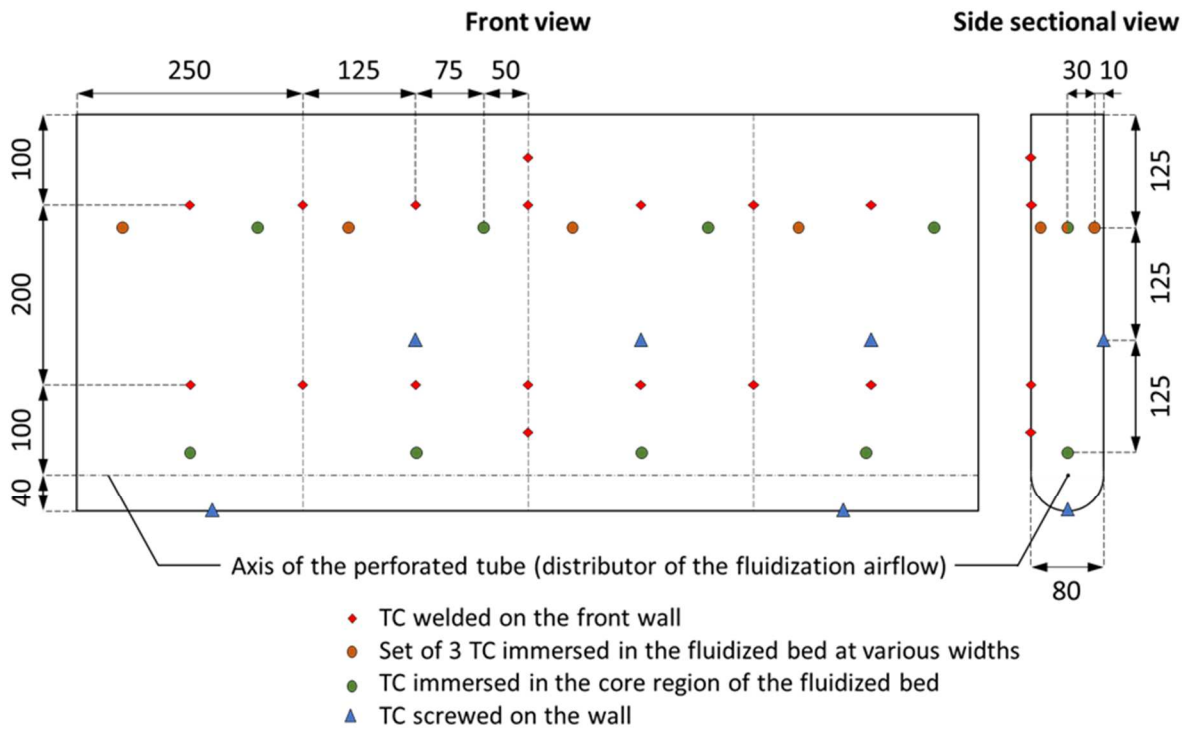

Figure 5. Schematic of the reactor showing the position of the thermocouples (dimensions in mm).

There were 16 thermocouples spot-welded on the front wall of the reactor-receiver (see Fig. 6). They were mainly used during operation to ensure that overheating did not occur (reactor wall should not exceed 1100 °C at any location) and to estimate the wall temperature distribution. On the back and at the bottom of the reactor, five thermocouples were screwed in and enabled for calculating the energy balance of the reactor. Inside the fluidized bed reactor, 20 thermocouples were implemented through ports at various depths and widths in each compartment in order to strictly monitor the temperature of the fluidized bed, as shown in Figure 5. All these thermocouples allowed the determination of a representative average temperature of the bed, characterization of the thermal homogeneity of the reactor, and measurement of thermal gradients due to heat transfers in the fluidized bed.

In addition, thermocouples were located at key points of the loop: in the fluidization air before and after preheating, exhaust gas before and after the cooler, fines from the cyclone, and particles in the cold and hot tanks.

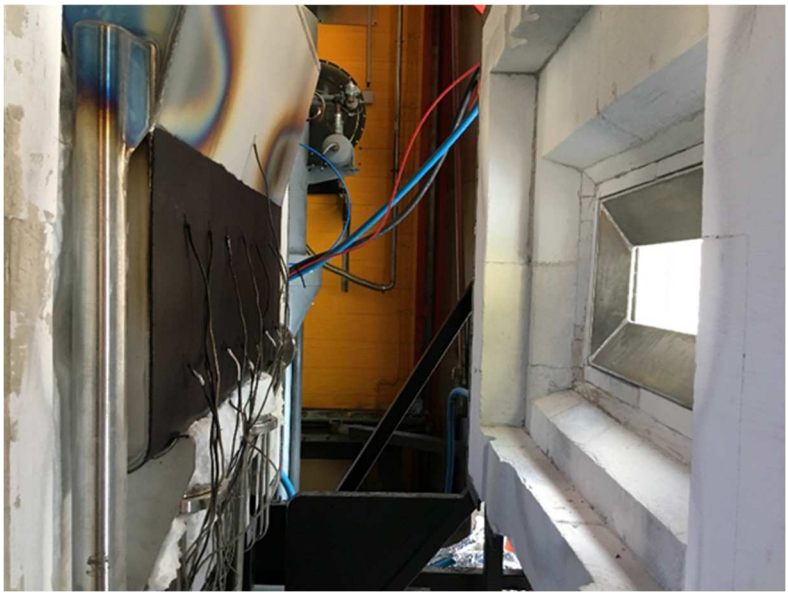

Figure 6. View of the reactor (left) inside the cavity with the welded thermocouple on the front wall. Right side is the water-cooled aperture and the inner insulation.

Five pressure sensors were located at various heights in the reactor. An additional pressure sensor was located at the inlet of the air distributor in order to calculate the physical properties of the fluidization air.

The mass flow of the fluidization air was measured by a Kobold KME thermal flow sensor (accuracy ± 3% of reading + ± 0.6 sm^3/h). The mass flow and the physical properties (pressure and temperature) of fluidization air determined the average gas velocity in the reactor. It ranged from 0.15 to 0.40 m/s. The air mass flow was controlled by using a needle valve in order to reach the set value. Usually, a mass flow corresponding to 5 to 10 times the minimum fluidization velocity of the particles was set in the reactor.

All the measuring instruments were connected to a data logger, Graphtec midi Logger GL800, that was connected to a laptop. The measuring data were recorded with a frequency of 1 Hz through a dedicated software developed with LabVIEW.

Control of solar flux distribution, aiming strategy

Ideally, a homogenous incident concentrated flux is delivered by the solar facility to avoid hot spots on the receiver that would damage or even destroy the reactor However, as all solar furnaces, the 1 MW solar furnace was designed to achieve very high peak fluxes on a small surface, as opposed to a homogenous flux on a large surface, such as the SOLPART receiver. Each of the 63 heliostats delivers nearly the same power on the focal plane, but their peak flux density ranges from 15 to 330 suns, and their beam incident angles range from 15 to 75° due to their relative location in the field compared to the parabola and its optical axis. By aiming each heliostat at a different location instead of the nominal focal point, these power distribution

differences can be used to control the flux distribution on the setup. However, the use of a cavity makes it difficult to determine the aiming location, as a small offset of a heliostat at the focal plane may move its beam suddenly inside or outside the cavity. The cavity aperture acts as an optical diaphragm, or a letterbox, through which the appropriate flux at the appropriate location must be controlled (Fig. 7). In addition, the size of the effective aperture may change by moving the shutter placed in front of the main cavity aperture.

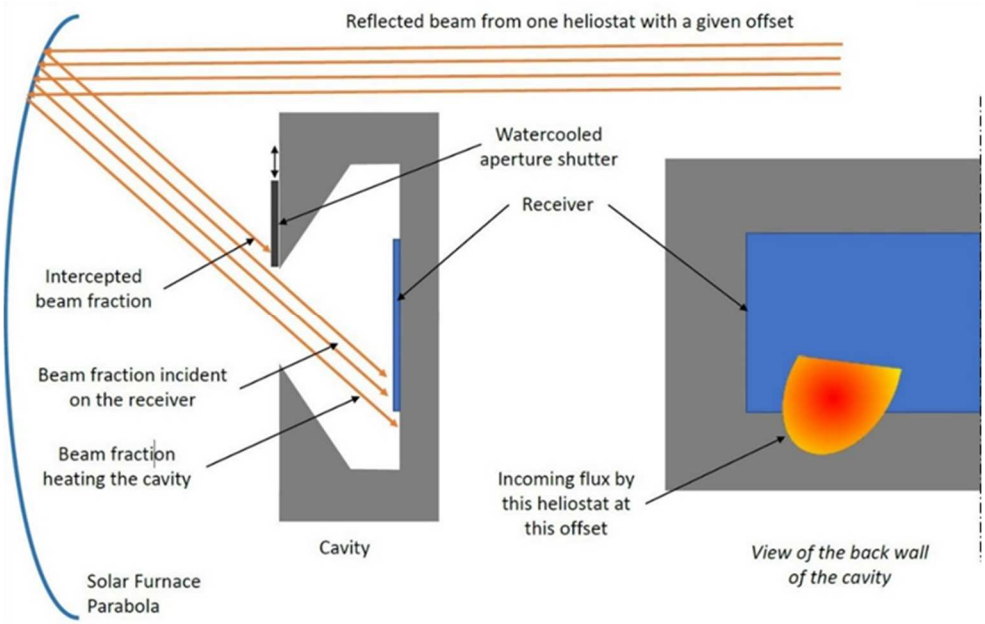

Figure 7. Simplified cross-sectional view with a beam reflected by a heliostat being intercepted by the cavity aperture and partially impacting the receiver (left), also seen on the back wall of the cavity (right).

Notably not depicted here: the additional beam interceptions by the doors of the solar furnace.

The problem was solved using a hybrid simulation-experimental method. The flux distribution on the reactor front wall for each heliostat at each considered offset location (heliostat flux distribution with offsets database) was measured to create a database. Then, a simulation tool was created to select the heliostat configurations in this database to reach the targeted mean flux density with a given constraint on the minimum and maximum local flux density (to avoid hot spots) and the standard flux deviation (to represent homogeneity).

To produce the flux distribution database, each heliostat was scanned at the focal plane, and the actual flux distribution inside a mockup cavity (a diffusive-reflective target placed at the location of the reactor) was measured with a calibrated camera (Fig. 8).

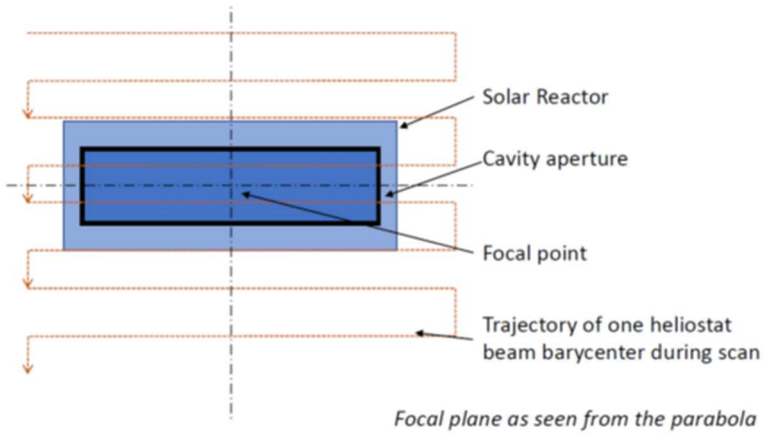

Figure 8. Principle of the scan of each heliostat on the focal plane to build the flux database as a function of the heliostat offsets.

The camera-based flux measurement system was adapted in order to cope with the camera installed inside the cavity, which used a fisheye lens that produced strong optical aberrations requiring adapted correction. The camera required an internal instead of an external position because it was impossible to see the complete receiver front wall through the smaller cavity aperture.

Two calibrations were needed to use the camera as a radiometric measurement device.

- Spatial calibration. A reference checkerboard was placed on the receiver in order to determine the optical aberrations and the perspective effect due to the fisheye lens and the installation of the camera inside the cavity. A simplified algorithm was used, as it was sufficient to deliver the low-resolution flux map needed for the next steps (25x25 mm final resolution).
- Radiometric calibration. This was done using a reference radiometer sensor (Vatell 25 mm) installed at the center of the Lambertian receiver in the mockup cavity. This sensor allowed the conversion from brightness (gray levels) to flux density measurements (kW/m^2 or suns). The brightness homogeneity of the fisheye lens was evaluated before this conversion using diffuse lighting of the cavity, with the heliostats reflecting the solar radiation at the bottom of the parabola (simplified white box setup).

The data processing steps are summarized in Figure 9. Thirty-five heliostats were selected to establish the database based on their incident beam angle.

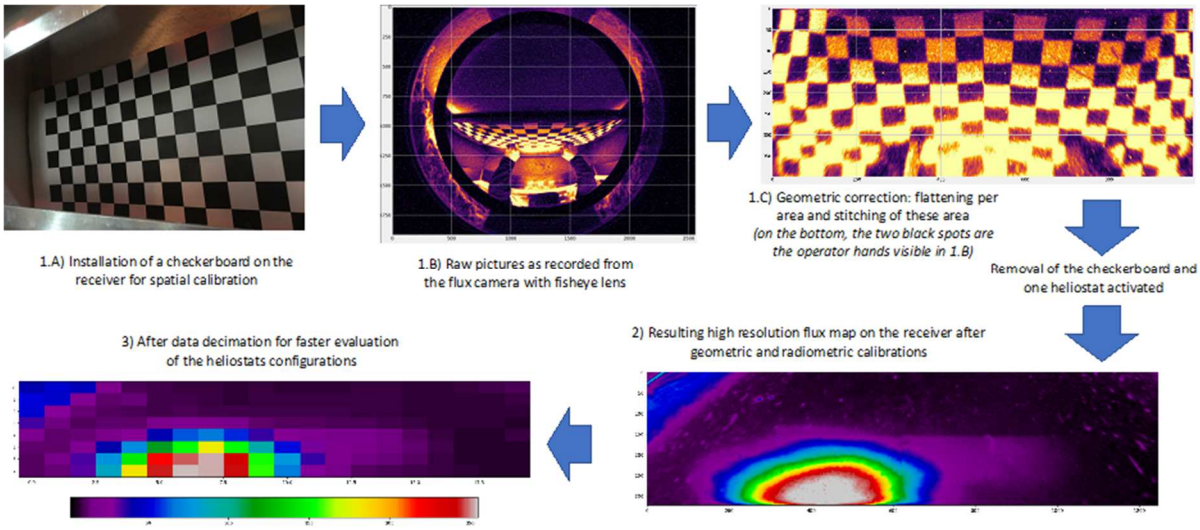

Figure 9. Sample case of the data processing of the flux measurement system with a fisheye lens for the aiming strategy determination: 1) spatial calibration by means of a reference checkerboard 2) radiometric calibration with the reference radiometer installed at the center of the receiver 3) data decimation to simplify the post processing and aiming strategy determination

A genetic algorithm was selected and implemented to determine the best heliostat offset configurations using the experimental database. A large number of significantly different configurations with the best statistical performance were identified. The performance was evaluated with the mean flux level and the flux homogeneity on the receiver. Approximately 2000 configurations, for all flux levels, were finally considered, along with 3 different positions of the cavity aperture shutter. Even if the configurations discovered with the evolutionary algorithm exhibited a satisfactory homogeneity, the average thermal homogeneity on the receiver was further improved by cycling between different heliostat configurations that had similar statistical performances (mean and standard deviation) but different heliostat aiming configurations (temporal dithering). Since the location of the hot and cold spots differed between these configurations, changing the aiming configurations resulted in smoothing temperature difference over time to achieve better mean spatial and temporal average temperatures using the thermal inertia of the receiver. This was achieved by changing quickly between the configurations, every 15 seconds. As an example, two solar flux density distributions (processed images from the camera) that correspond to an average concentration of 215 suns are illustrated in Figure 10.

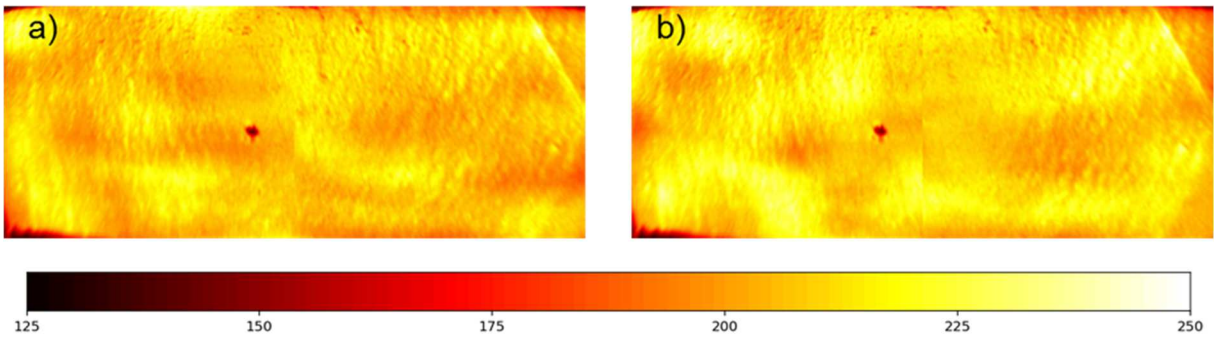

Figure 10. Distribution of the flux density of two heliostat configurations giving an average concentration factor (C) of 215. a) 139 < C < 237 (σ = 12.5). b) 150 < C < 239 (σ = 14.5). The central point corresponds to the fluxmeter. The colormap is the OpenCV "hot" palette: from 125 suns (black) to 250 suns (white), with red (175 suns) and yellow (225 suns) in between.

Particles

The decomposition of calcite aims to produce quicklime by removing the carbon dioxide: $CaCO_3 \rightarrow CaO + CO_2$. This calcination reaction typically occurs at approximately 850-950°C, depending on the CO_2 partial pressure (the higher the CO_2 partial pressure, the higher the temperature of reaction) (Valverde, 2015).

The calcite used during the tests was supplied by the company La Provençale from the quarry of Espira-del'Agly in France. This industrial feedstock was directly used without pretreatment. Measurements of the mass loss ratio after complete calcination of several samples (at 950 °C for 3 hours) showed that the fresh raw material consisted of 98.5% to 100% $CaCO_3$, with the remaining part consisting of nonreactive materials. In a conservative approach, a mass loss ratio corresponding to 98.5% $CaCO_3$ was considered to calculate the degree of conversion.

The particle size distribution of the fresh raw material was analyzed twice during the test campaign. The results are reported in Figure 11. The results of the two measurements are not identical because of the variability of the raw material. In both cases, Figure 11 shows the relatively high fraction of fine particles (approximately 10% of the volume fraction with a diameter less than 10 µm). Considering the Sauter mean diameter d_{sv} of the particles and the density of calcite, which is 2710 kg/m^3, the particles are classified as C-type particles (cohesive) according to the Geldart classification (Geldart, 1973). Indeed, this does not correspond to the experimental observations during the fluidization tests. Considering the average volume diameter d_v of the particles instead of the Sauter mean diameter, the particles are classified as between A-type (aeratable) and B-type (bubbling) particles. This corresponds better to the experimental observations.

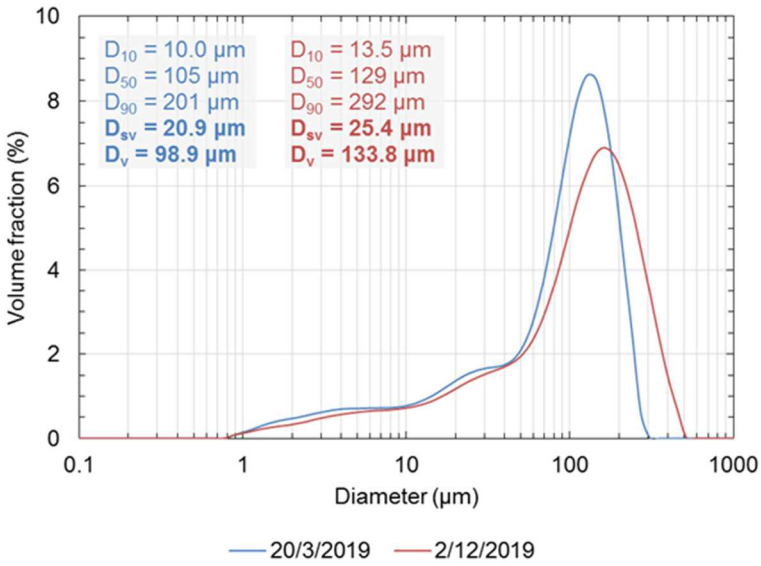

Figure 11. Particle size distribution of the calcite used during the tests.

The minimum superficial fluidization velocity of the particles at ambient temperature and pressure (~20 °C, 840 hPa) was measured experimentally. Three tests gave an average value of 8.8 mm/s. By using the average evolution of the minimum fluidization velocity as a function of the temperature predicted by several correlations from the literature (Broadhurst and Becker, 1975; Thonglimp et al., 1984; Wen and Yu, 1966), it is possible to extrapolate the measured value at high temperature. Thus, a minimum fluidization velocity of 8.8 mm/s at 20°C corresponds to a minimum fluidization velocity of 4.0 mm/s at 800 °C. In addition, the fluidization of the particles was tested in a transparent mockup of the solar reactor. These tests resulted in determination of the minimum airflow rate that ensured a good circulation of the particles. At ambient temperature, a fluidization flow rate corresponding to at least 5 times the minimum fluidization velocity was required.

3. Test results

Operation procedure

Typical solar tests lasted from four to six hours. A test consisted of two consecutive phases: first, the reactor filled with particles was heated until the fluidized bed reached the temperature of reaction; then, the reactor was fed with the appropriate mass flow rate of particles until a steady state was reached. During the test, the critical operating parameter was the opening of the cavity aperture. At the beginning of the heating period, the cavity's shutter was opened progressively to avoid thermal shocks. Then, the shutter position was controlled to maintain the indicated front wall temperature between 950 and 1050 °C. The position of the shutter was

adapted to compensate the daily variations of the direct normal irradiance (DNI) in order to maintain a stable temperature level on the reactor front wall and, consequently, inside the fluidized bed compartments. Stable chemical conversion of the fluidized particles was proportional to the mean residence time of the particles in the reactor, τ (i.e., to the particle inlet mass flow rate). Consequently, when a stable particle temperature was maintained during the characteristic time τ, the conversion degree at the reactor outlet reached the equilibrium value. In addition, the stability of the CO_2 content in the exhaust gases was a very sensitive indicator to assess the evolution of the calcination reaction.

The rigorous assessment of the steady-state regime could only be ascertained after the test, with the analysis of the particles sampled at the exit of the reactor. Obviously, steady-state regime corresponded to a constant degree of conversion in consecutive samples.

The degree of conversion of the samples taken at the reactor outlet was determined by complete calcination. The mass loss experienced by the sample after its complete calcination in an electrical furnace was compared to the mass loss experienced by a reference sample of initial particles taken at the reactor inlet. The complete calcination was carried out by heating the samples at 950 °C for 3 hours. The degree of conversion is given by Equation (1).

$$\alpha = 1 - \frac{\frac{m_s}{m_f} - 1}{\frac{m_{ref,0}}{m_{ref,f}} - 1} \qquad (1)$$

In this equation, m_s is the mass of the analyzed sample taken at the reactor outlet, m_f is the final mass of the sample after complete calcination in an electrical furnace, $m_{ref,0}$ is the mass of a reference sample of raw calcite taken at the reactor inlet, and $m_{ref,f}$ is the final mass of the reference sample after complete calcination in the electrical furnace.

Experimental results

The effects of two main parameters, i.e., the fluidization conditions (air mass flow rate) and the particle mass flow rate, on the conversion degree was examined. One cannot consider the particle temperature as a parameter because it is the result of the constraint on the maximum acceptable wall temperature.

During the tests, particular attention was paid to the heating period of the reactor in order to reduce the time during which no calcination reaction occurred, as the particle temperature was too low. A key factor that governed the dynamic thermal behavior of the solar reactor was the fluidization velocity. Figure 12 plots the variations of the mean temperature in the four compartments of the solar reactor, the maximum temperature of the reactor's front wall, the degree of aperture of the solar cavity and the DNI with time for one typical experiment. The mean temperature in the compartments corresponds to the arithmetic average of the

temperature as measured by all the thermocouples immersed in the fluidized bed of particles (orange and green dots of Figure 5).

Figure 12 indicates that the heating period duration was less than one hour and that the temperature difference between the compartments was very small. The particles were injected approximately 45 min after the starting of the experiment, when the CO_2 analyzer indicated a significant increase in the CO_2 content in the flue gas. The equilibrium temperature was then reached after approximately 30 min.

Figure 12 also shows how the mean particle temperature was maintained through the variation of the shutter position. The variation of DNI at 10:45 was compensated by the opening of the shutter that resulted in an increase of the solar power entering the cavity. The shutter was then gradually closed to follow the DNI increase.

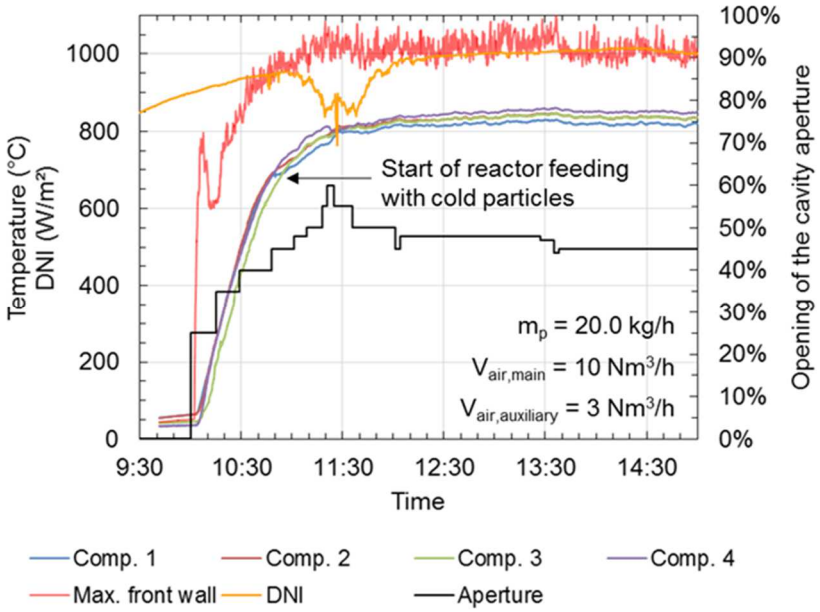

Figure 12. Variations of main operation parameters with time during a typical experiment.

The sensitivity of the CO_2 analyzer to the fluidized bed temperature is illustrated in Figure 13. At the beginning of the sequence, the CO_2 mole fraction increases to reach the equilibrium value corresponding to the mean temperature (at approximately 15:50). Then, the CO_2 analyzer follows the variation of the temperature, resulting in the change of the calcination reaction kinetics.

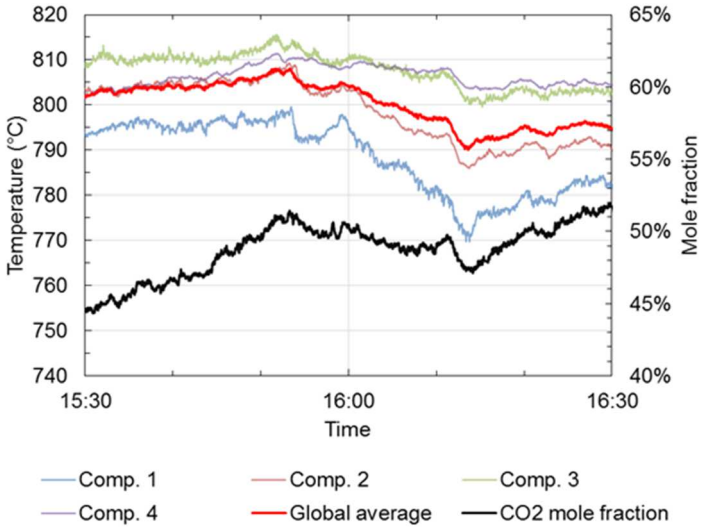

Figure 13. Response of the CO_2 analyzer to the temperature variation of the four compartments of the solar fluidized bed.

Table 1 lists the operation parameters and the main results of the six representative experimental tests. The particle mass flow rate and the solar power varied from 14.5 to 25.1 kg/h and from 45.4 to 64.4 kW, respectively. The maximum degree of conversion was 95.2% at 20 kg/h and 57.8 kW (solar power). Surprisingly, the degree of conversion of the test at 20 kg/h and low fluidization velocity exhibited a higher mean particle temperature but a lower degree of conversion than the test at high fluidization velocity. Two phenomena may contribute to this result: the CO_2 partial pressure and the insufficient mixing of particles. At low fluidization flow rate, the CO_2 partial pressure in the reactor is higher than at high fluidization flow rate, and the mixing of particles in the compartment is weak, resulting in a larger thermal gradient inside the bed of particles. In particular, the particle temperature is much higher than the mean temperature very near the irradiated wall, but the temperature is 100°C or more lower near the back wall under these conditions. Both phenomena contribute to a lower degree of conversion, even at a higher mean temperature.

Table 1. Main experimental results of the test campaign.

F_p (kg/h)	$F_{air,main}$ (Nm^3/h)	$F_{air,auxiliary}$ (Nm^3/h)	DNI mean (W/m^2)	C mean	Aperture	P_{in} (kW)	T_p (°C) Global average	$T_{w,max}$ (°C)	α_{out}
14.5	10.1	0	970	220	33.0%	45.4	818	1108	94.1%
14.5	14.0	3	777	220	52.5%	58.4	813	972	90.8%
20.0	10.1	3	1000	220	48.0%	67.4	831	997	88.5%
20.0	19.3	4	927	220	45.0%	57.8	813	1022	95.2%
25.1	12.3	3	962	220	42.5%	55.9	790	949	40.5%

25.1	19.6	4	768	220	65.0%	64.4	804	1063	77.5%

For each particle mass flow rate, two fluidization conditions (low and high fluidization velocity) have been tested. Because the other operation parameters could not be kept identical from one test to the other, the data do not enable clear identification of a single influence of the fluidization flow rate. However, during the tests, it was observed that increasing the fluidization flow rate improves the mixing and the circulation of the particles and hence the thermal homogeneity of the fluidized bed. Increased fluidization also improves the heat transfer coefficient of the particles and allows increased incident solar power on the reactor's front wall without overheating. Moreover, from a theoretical point of view, a high fluidization flow rate reduces the partial pressure of CO_2 in the fluidized bed and promotes the calcination reaction. However, at high fluidization flow rate, a larger proportion of the particles was recovered in the filter. This proportion was approximately 20% and 50% respectively at low and high fluidization flow rates. These relatively high proportions were probably caused by the undersizing and clogging of the cyclone. Consequently, for future applications, specific attention should be paid to the design of the dust extracting system.

The next figures illustrate the test results. Figure 14 plots, for the best result (20 kg/h, high fluidization velocity), the time variation of the DNI, the compartment temperatures, the maximum front wall temperature, the CO_2 mole fraction, and the calcination degree. The calcination degree is not zero at the beginning of the test because the run started with the calcite-lime mixture resulting from the previous run. The chemical conversion stabilized approximately 2 h after the starting of particle feeding that corresponds to the mean residence time of the feedstock inside the reactor. The time during which the particles were fed in the reactor is shown in gray. The feeding was stopped after a few minutes, at 13:54, due to a minor technical problem. As a result, a small increase in the conversion degree was observed just after this event (97%); then it stabilized at the mean value (95%).

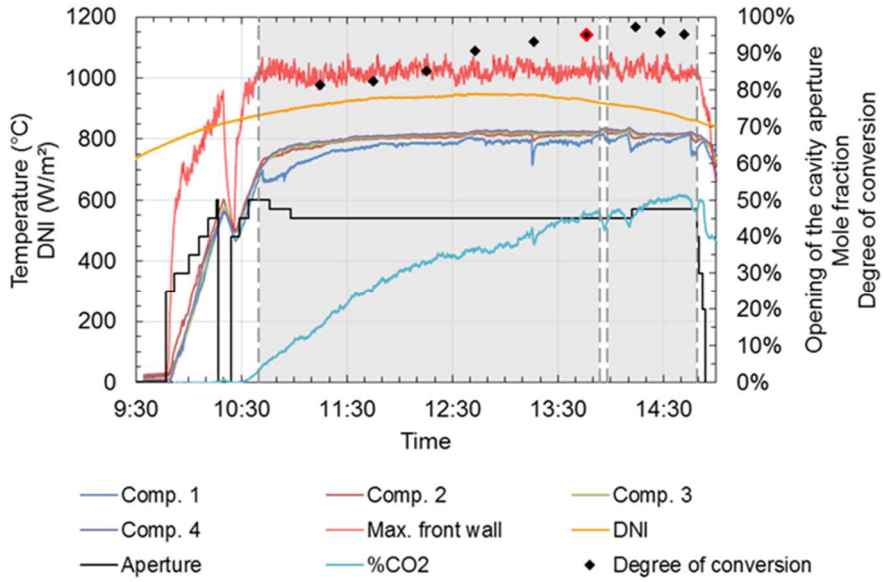

Figure 14. Time evolution of the operating parameters and results. Calcite 20.0 kg/h, high fluidization flow rate. Gray area: feeding of the reactor with particles. Red dot: degree of conversion corresponding to steady-state regime.

Figure 15 shows the temperature profile inside the compartments along the reactor depth (8 cm). The mean temperatures and temperature profiles were very close in the four compartments. The particle temperature near the front wall ranged from 825 °C to 858 °C, and the maximum temperature difference was less than 115 °C between the front and back of the fluidized bed. This result indicates the efficient mixing of the particles.

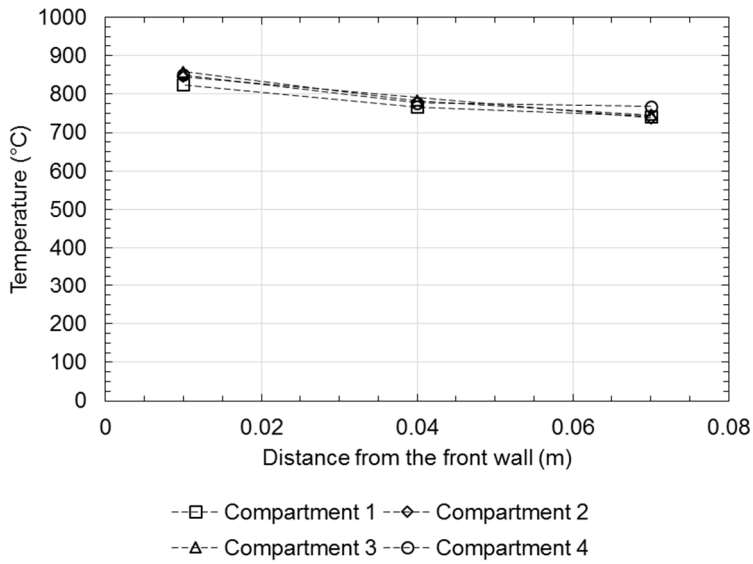

Figure 15. Temperature profile inside the fluidized particles. Calcite 20.0 kg/h, high fluidization flow rate.

The inlet mass flow rate of particles influenced the mean residence time of the particles in the reactor. From a theoretical point of view, the higher the residence time, the higher the outlet degree of conversion. However, the results of the test campaign showed that the mass flow rate of particles had a second-order influence on the outlet degree of conversion in the mass flow rate range of 5-20 kg/h. The first-order parameter was the temperature, as illustrated in Figure 16, which illustrates the variation of the degree of conversion with mean particle temperature. In the temperature range tested, 790–832 °C, there is a strong effect of the global average particle temperature (accounting for the four compartments) on the calcite conversion. This result indicates the sensitivity of the reaction kinetics with temperature.

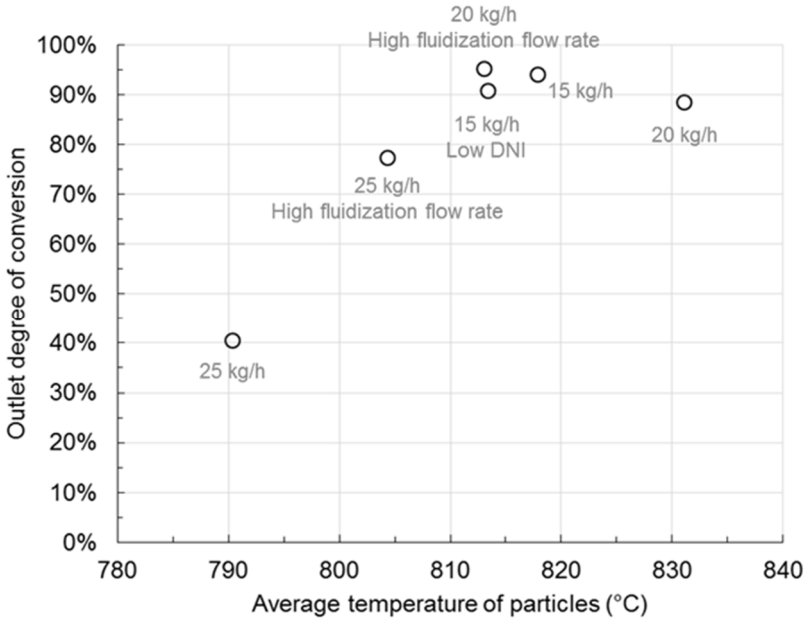

Figure 16. Degree of conversion of calcite (at steady state) as a function of the global average temperature of the particles in the reactor.

4. Result analysis

The experimental study was completed with the analysis of the produced lime, reactor thermal, and thermochemical performances.

The chemical composition of the product and BET surface area are listed in Table 2.

Table 2. Chemical and physical analysis of the produced lime (composition in mass fraction)

Composition/ Characteristics	15 kg/h	15 kg/h low DNI	20 kg/h low fluidization flow rate	20 kg/h high fluidization flow rate
CaO	90.52%	82.72%	80.65%	91.24%
$CaCO_3$	8.45%	16.39%	18.60%	7.62%
CO_2	3.72%	7.21%	8.18%	3.35%
SiO_2	0.182%	0.141%	0.120%	0.140%
Fe_2O_3	0.061%	0.070%	0.050%	0.080%
Al_2O_3	0.131%	0.080%	0.090%	0.070%
MgO	0.514%	0.402%	0.450%	0.672%
MnO	0.002%	0.002%	0.002%	0.023%
S	0.001%	0.001%	0.002%	0.015%
$\alpha_{composition}$	94.9%	90.8%	88.3%	95.5%
$\alpha_{mass\ loss}$	94.1%	90.8%	88.5%	95.2%
SS (m^2/g)	3.84	5.15	5.00	5.39

The chemical composition of the samples was determined by means of the X-ray fluorescence method. The accuracy of this method is estimated to be ±1%. The CO_2 mass fraction indicated in Table 2 corresponds to the CO_2 present in the form of $CaCO_3$ and enables the validation of the degree of calcination in the samples in addition to mass loss. The conversion degree $\alpha_{composition}$ of the samples was calculated from the chemical composition. The uncertainties of measurement of the conversion degree $\alpha_{mass\ loss}$ calculated with the mass loss method is less than ±2% absolute. Considering these uncertainties, Table 2 indicates a very good agreement between the degree of conversion obtained from the chemical composition and the mass loss. In addition, the BET surface area is high (approximately 5 g/m^2), indicating a high reactivity of the product.

Two efficiencies are defined: The thermochemical efficiency (η_{thch}) considers only the enthalpy of reaction, while the thermal efficiency (η_{th}) accounts for the enthalpy of reaction and the power provided to heat the particles and the fluidization gases. They are defined as the ratio of these values to the gross incident solar power through the cavity aperture (P_{in}). The efficiencies are calculated at steady state. The thermal power consumed to preheat the fluidization air is not considered in the calculation because, in a commercial application, this power will be supplied by recovering the waste heat of exhaust gases. Nevertheless, the increase of air enthalpy is

calculated using the inlet air temperature after the preheater. The efficiencies are defined as follows:

$$\eta_{thch} = \frac{P_{reaction}}{P_{in}} = \frac{x_{CaCO_3,0} \cdot \dot{m}_p \cdot \alpha_{out} \cdot M_{CaCO_3} \cdot \Delta H_{R,CaCO_3 \rightarrow CaO + CO_2}(T_{p,mean})}{P_{in}} \quad (2)$$

$$\eta_{th} = \frac{P_{reaction} + \dot{m}_p \cdot h_{CaCO_3}^{T_{in} \rightarrow T_{p,mean}} + \dot{m}_{air,main} \cdot h_{air}^{700°C \rightarrow T_{p,mean}} + \dot{m}_{air,auxiliary} \cdot h_{air}^{10°C \rightarrow T_{p,mean}}}{P_{in}} \quad (3)$$

In these equations, $x_{CaCO3,0}$ is the mass fraction of calcium carbonate at the reactor inlet, $\dot{m}_p$ is the inlet mass flow rate of particles, α_{out} is the degree of conversion measured at the reactor outlet, M_{CaCO3} is the molar mass of calcium carbonate (100.087 g/mol), $T_{p,mean}$ is the average temperature of particle in the reactor, P_{in} is the solar power entering the cavity, $\dot{m}_{air,main}$ and $\dot{m}_{air,auxiliary}$ are respectively the mass flow rates of the main and the auxiliary fluidization airflows, and $h^{T1 \rightarrow T2}$ is the difference of specific enthalpy between the temperatures T_1 and T_2. Then,

$$\Delta H_{R,CaCO_3 \rightarrow CaO + CO_2} = -1.447 \cdot 10^{-6} \cdot T^3 + 3.323 \cdot 10^{-3} \cdot T^2 + 5.882 \cdot T + 1.810 \cdot 10^5 \quad (4)$$

$$h_{CaCO_3}(T) = 9.963 \cdot 10^2 \cdot T + 1.345 \cdot 10^{-1} \cdot T^2 + 5.882 \cdot T + \frac{2.156 \cdot 10^7}{T} \quad (5)$$

$$h_{air}(T) = 1.041 \cdot 10^3 \cdot T - 1.512 \cdot 10^{-1} \cdot T^2 + 2.500 \cdot 10^{-4} \cdot T^3 - 9.883 \cdot 10^{-8} \cdot T^4 + 6.782 \cdot 10^{-12} \cdot T^5 + 2.686 \cdot 10^{-15} \cdot T^6 \quad (6)$$

The enthalpy of the calcination reaction was calculated by assuming that the reaction occurred in the whole reactor at the average temperature of particle. The enthalpy of reaction ΔH_R is given in Joule per mole of $CaCO_3$ by Equation (4), with the temperature T expressed in Kelvin. This formula was obtained by regression of the tabulated variations of enthalpy for the reaction $CaCO_3 \rightarrow CaO + CO_2$, calculated with the data from Robie and Hemingway, 1995. For example, this equation shows 0.525 kWh/kg of $CaCO_3$ converted at 800 °C.

In Equations (5) and (6) the coefficients are respectively taken from Robie and Hemingway, 1995, and Hilsenrath et al., 1955.

The solar power entering the cavity was calculated with data processing of measurements at the cavity aperture. For each configuration of heliostats, the whole range of aperture degree of the cavity was considered. The power was calculated every 5%, from 0% to 100% of aperture, and interpolations were used in between. All the configurations of heliostats potentially used during a test were simulated (due to the temporal dithering method, many configurations are used during one single test). Then, the results were averaged in order to obtain a mean solar power, depending on the concentration factor and the opening of the cavity aperture (surface area of the aperture).

Figure 17 shows the distribution of the solar power entering the cavity between the power used for the calcination reaction, the overall power transferred to the particles and the gas, and the thermal losses. The data corresponded to steady state when the outlet degree of conversion stabilized. The uncertainty on the data is estimated to be 10%. This power typically ranges from 45 kW to 65 kW. Considering the inlet mass flow rate of particles and the outlet degree of conversion, the heat consumed by the reaction typically ranges from 6.8 kW to 10.1 kW, except for the test at 25 kg/h (in standard conditions), which exhibits a low degree of conversion. Consequently, the calculated thermochemical efficiency ranges from 12% to 17% (9% for the test at 25 kg/h). By considering the sensible heat provided to the particles and the fluidization air, the total useful energy ranges from 11 kW to 18 kW. Consequently, the thermal efficiency ranges from 21% to 29%. The enthalpy of reaction represents from 55% to 63% of the useful energy (42% for the test at 25 kg/h).

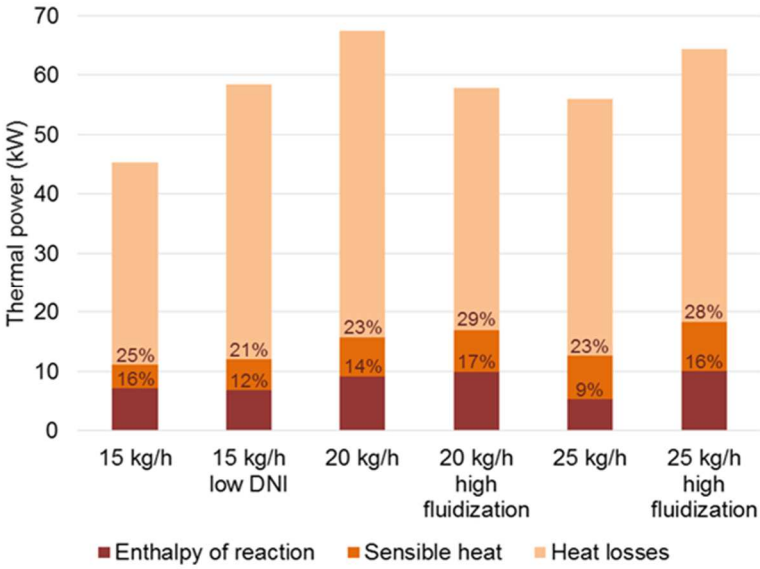

Figure 17. Distribution of the solar thermal power entering the cavity and corresponding thermal and thermochemical efficiencies at steady state.

Finally, the best result was obtained for a calcite mass flow rate of 20 kg/h, resulting in a degree of conversion of 95.2%, a BET surface area of the lime of 5.39 m^2/g, and 17% and 29% thermochemical and thermal efficiency of the reactor, respectively.

5. Discussion

This section presents comments on the applications of lime and quality standards, the management of CO_2, and scaling-up issues of the solar process.

Applications of lime are broad, and the relative importance of each industry varies heavily from one country to another. The main application domains are the iron and steel industry,

environmental protection, construction materials, civil engineering, the chemical industry, and agriculture. For example, 40% of lime in Europe is used in the steel industry (EuLA, 2020). It is obvious that lime quality criteria depend on the application domain. Expected properties are chemical purity, color, reactivity with water and gases (quicklime), mechanical behavior (in particular compressive strength), mean particle size, particle size distribution, and others. The standard for CaO content in the product is not the same for applications in the steel industry as it is for construction materials. The mean CaO content is 95% (93% minimum) for steel making, approximately 92% for water treatment, and 98% for construction materials (Oates, 1998). Specific standards have been published in each application domain. For example, the EN 459-2 standard defines the test to measure quicklime reactivity for construction applications.

Lime reactivity depends on material porosity and BET specific surface area. Commandré et al. (2007) reported a complete study of lime reactivity as a function of calcination temperature and CO_2 partial pressure. They showed that the reactivity varies dramatically with both parameters. Lime produced at 600 °C and 750 °C in laboratory conditions under nitrogen exhibited a specific surface area of 80 m^2/g and 30 m^2/g, respectively. Heating the sample up to 1100 °C caused a reduction of the surface area to 1.65 m^2/g and 1.15 m^2/g under N_2 and CO_2, respectively. The loss in reactivity due to CO_2 partial pressure is known as “chemical sintering,” which is similar to thermal sintering due to temperature. In industrial lime kilns, the feedstock experiences temperature in the range of 1100-1300 °C that results in sintering of the product. Consequently, BET surface areas of limes produced by shaft kilns and rotary kilns are less than 1 m^2/g and 2 m^2/g respectively. Fluidized bed kilns only produce lime with specific surface areas equal or larger than 2 m^2/g because they operate at lower temperatures. This type of quicklime is named “highly reactive” (Dheilly et al., 1998).

Carbon dioxide content in the reactor during calcination appears to be a key process parameter. On the one hand, increasing the CO_2 partial pressure results in a decrease of the calcination kinetics at a given temperature and a reduction of product reactivity. On the other hand, it should be of interest to operate under 100% CO_2 in order to produce a pure CO_2 flue gas that can be sequestered and used in the chemical industry. The fluidized bed technology allows a choice of the operation conditions that fit with the targeted application because fluidization gas can be changed from air to CO_2. Consequently, the choice of the operation conditions is a result of a compromise between solid product properties and utilization of process gas.

This paper demonstrates the capacity of multistage horizontal fluidization to achieve pilot-scale calcination of limestone in continuous mode. The next step will be the scaling up of the

technology to the MW scale with a reactor efficiency similar to that of industrial kilns. In commercial lime kilns, the feedstock (limestone, $CaCO_3$) is heated from ambient temperature to above 800 °C in the preheating zone by the gas leaving the calcination zone. This corresponds to the internal heat recovery. The overall heat requirement for the process (heating and chemical reaction) is 4900 kJ/kg CaO, with two-thirds (62%) corresponding to the calcination reaction. The thermochemical efficiency (100% corresponding to a heat consumption of 3060 kJ/kg CaO) of commercial lime kilns was discussed in Oates (1998). This efficiency varies strongly with the type of kiln. For long rotary kilns, it ranges from 40 to 50%, while it reaches 77-90% for modern shaft kilns. Fluidized bed industrial lime kilns exhibit a medium thermochemical efficiency of approximately 60%. The challenges concerning heat recovery differ widely between the standard and the solar kilns. In standard lime kilns, the exhaust gas contains more heat than is required to preheat the feedstock, and the product (lime) does not contain enough energy to preheat the combustion air (Oates, 1998). In the solar kiln, the exhaust gas does not contain enough energy to preheat the feedstock but contains more heat than is necessary to preheat the fluidization gas. Consequently, it is necessary to recover heat from the hot product in order to preheat both the limestone and the fluidization gas. Heat recovery from the hot product can be performed in a secondary fluidized bed located at the exit of the solid product (lime outlet). The produced hot air from this direct contact heat exchanger and the exhaust gas from the solar reactor is used for the preheating of both the limestone and the fluidization air.

A demo-scale (MW scale) fluidized bed calcination solar reactor can target a thermochemical efficiency similar to an industrial fossil-fueled fluidized bed kiln (approximately 60%), using heat recovery as explained in the previous paragraph. A cavity-type solar reactor operating with an irradiated wall at 1000 °C and an irradiated surface area and aperture surface area ratio of 2 experiences 30% radiation loss (dominant mode of heat loss). This accounts for our experimental results that reveal the mean solar flux density on the reactor wall will be approximately 250 kW/m^2 and the mean solar flux density at the aperture will be 500 kW/m^2. The MW-scale solar reactor will consist of the assembly of four 1x1 m single-stage fluidized bed modules working in series. This design allows the same residence time distribution of particles that was achieved in the pilot-scale solar reactor. At commercial scale, a 40 MW solar reactor can produce 300 tons/day of quicklime. Considering the application of the solar technology at an industrial scale, two issues must be considered: maintaining product quality (conversion degree) and designing a 24 h-per-day process. The former issue can be addressed by adding a maturing reactor in series with the solar reactor. This reactor can be heated by fuel since the energy requirement is very small with respect to the solar part. The latter issue can be addressed by the implementation of a hybrid process in which the thermal

energy is provided by concentrated solar and combustion heat sources. Clean combustion heat sources can be either hydrogen or biomethane. In addition to lime production, the fluidized bed solar technology can be applied to thermochemical energy storage, since this calcination process produced highly reactive quicklime.

6. Conclusion

This paper demonstrates the successful scaling up of the horizontal multistage solar fluidized-bed concept at pilot scale for calcination. The on-sun operation of the system with a mean flux density of 220 suns indicates the sensitivity of the reactor to the fluidization conditions and the solar flux distribution on the solar-irradiated wall. The efficient mixing of fluidized particles results in an effective wall-to-fluidized bed heat transfer that allows a mean wall-to-particle temperature difference of approximately 100°C and a temperature gradient of approximately 10°C/cm along the bed width. Moreover, the separation of the reactor in four sections narrows the residence time distribution of the particles. As a result, the product quality is constant and the conversion degree is high when a steady state is reached. For example, a conversion degree of 95% was obtained for a calcite mass flow rate of 20 kg/h and a mean overall bed temperature of 815°C. This achievement corresponds to a particle mass flow rate three times higher than the current state of the art for solar calcination. The next target is the demonstration of a 1-MW solar reactor operating either in solar-only mode (daytime) or in hybrid mode (24 h per day).

Acknowledgements

This project has received funding from the European Union's Horizon 2020 research and innovation program under grant agreement No. 654663, SOLPART project.
This work was supported by the French Investments for the Future program managed by the National Agency for Research under contract "ANR-10-EQPX-49-SOCRATE" (Equipex SOCRATE).
The authors thank Philippe Dumont (NLD) for providing the chemical analysis of the samples.

References

Broadhurst, T.E., Becker, H.A., 1975. Onset of fluidization and slugging in beds of uniform particles. AIChE Journal 21, 238–247. https://doi.org/10.1002/aic.690210204

Comessa, Thermal processing of bulk solids, www.comessa.com.

Commandre J-M., Salvador S., Nzihou A. (2007). Reactivity of laboratory and industrial limes. Chemical Engineering Research and Design, 85 (4): 473-480. 10.1205/cherd06200; hal-01634390

Dheilly, R.M., Tudo, J. and Queneudec, M., 1998, Influence of climatic conditions on the carbonation of quicklime, Journal of materials, Engineering and Performance, 7(6): 789–795.

Esence, T., Benoit, A., Poncin, D., Tessonneaud, M., Flamant, G., 2020. A shallow cross-flow fluidized-bed solar reactor for continuous calcination processes. Solar Energy 196, 389-398. https://doi.org/10.1016/j.solener.2019.12.029

EuLA, 2020, https://www.eula.eu/

Flamant, G., Hernandez, D., Bonet, C., Traverse, J.-P., 1980. Experimental aspects of the thermochemical conversion of solar energy; Decarbonation of CaCO3. Sol. Energy 24, 385–395. https://doi.org/10.1016/0038-092X(80)90301-1

Fletcher, E. A. and Moen, R. L., 1977. “Hydrogen- and oxygen from water,” Science 197(4308), 1050–1056.

Geldart, D., 1973. Types of gas fluidization. Powder Technology 7, 285–292. https://doi.org/10.1016/0032-5910(73)80037-3

Hilsenrath, J., Beckett, C.W., Benedict, W.S., Fano, L., Hoge, H.J., Masi, J.F., Nuttall, R.L., Touloukian, Y.S., Woolley, H.W., 1955. Tables of Thermal Properties of Gases, Comprising Tables of Thermodynamic and Transport Properties of Air, Argon, Carbon Dioxide, Carbon Monoxide Hydrogen, Nitrogen, Oxygen, and Steam (Circular No. 564). U.S. Department of Commerce, National Bureau of Standards.

Imhof, A., 2000. Calcination of limestone in a solar reactor. ZKG Int. 53, 504–509.

Imhof, A., 1997. Decomposition of limestone in a solar reactor. World Renew. Energy Congr. IV Renew. Energy Energy Effic. Environ. 10, 239–246. https://doi.org/10.1016/0960-1481(96)00072-9

Li, L., Coventry, J., Bader, R., Pye, J., and Lipiński, W., 2016. Optics of solar central receiver systems: a review. Optics Express, Vol. 24, No. 14, A985- A1007. https://DOI:10.1364/OE.24.00A985.

Meier, A., Bonaldi, E., Cella, G.M., Lipinski, W., Wuillemin, D., 2006. Solar chemical reactor technology for industrial production of lime. Sol. Energy 80, 1355–1362.

Moumin G., Tescari S., Sundarraj P., de Oliveira L., Roeb, M., Sattler C., 2019 Solar treatment of cohesive particles in a directly irradiated rotary kiln. Sol. Energy 182, 480–490. https://doi.org/10.1016/j.solener.2019.01.093

NF EN 459-2, 2012, Construction lime, Part 2: Test method.

Nikulshina, V., Halmann, M., Steinfeld, A., 2009. Coproduction of Syngas and Lime by Combined CaCO3-Calcination and CH4-Reforming Using a Particle-Flow Reactor Driven by Concentrated Solar Radiation. Energy Fuels 23, 6207–6212. https://doi.org/10.1021/ef9007246

Oates, J.A.H., 1998. Lime and Limestone: Chemistry and Technology, Production and Uses. Wiley-VCH.

Olivier, J.G.J., Janssens-Maenhout, G., Muntean, M., Peters, J.A.H.W., 2016. Trends in global CO2 emissions: 2016 Report. PBL Netherlands Environmental Assessment Agency

Robie, R.A. and Hemingway, B.S., 1995. Thermodynamic Properties of Minerals and Related Substances at 298.15 K and 1 Bar (10^5 Pascals) Pressure and at Higher Temperatures, U.S. Geological Survey Bulletin.

Steinfield, A., Imhof, A., Mischler, D., 1991. Experimental Investigation of an Atmospheric-Open Cyclone Solar Reactor for Solid-Gas Thermochemical Reactions. J. Sol. Energy Eng. Trans. ASME 114, 171–174. https://doi.org/10.1115/1.293000

Thonglimp, V., Hiquily, N., Laguerie, C., 1984. Vitesse minimale de fluidisation et expansion des couches fluidisées par un gaz. Powder Technology 38, 233–253. https://doi.org/10.1016/0032-5910(84)85006-8

Touloukian, Y.S., Dewitt, D.P., 1970. Thermal Radiative Properties: Metallic Elements and Alloys, Purdue Research Foundation. ed, Thermophysical Properties of Matter. New York - Washington.

Tregambi, C., Salatino, P., Solimene, R., Montagnaro, F., 2018. An experimental characterization of Calcium Looping integrated with concentrated solar power. Chem. Eng. J. 331, 794–802. https://doi.org/10.1016/j.cej.2017.08.068

Valverde, J.M., 2015. On the negative activation energy for limestone calcination at high temperatures nearby equilibrium. Chem. Eng. Sci. 132, 169–177. https://doi.org/10.1016/j.ces.2015.04.027
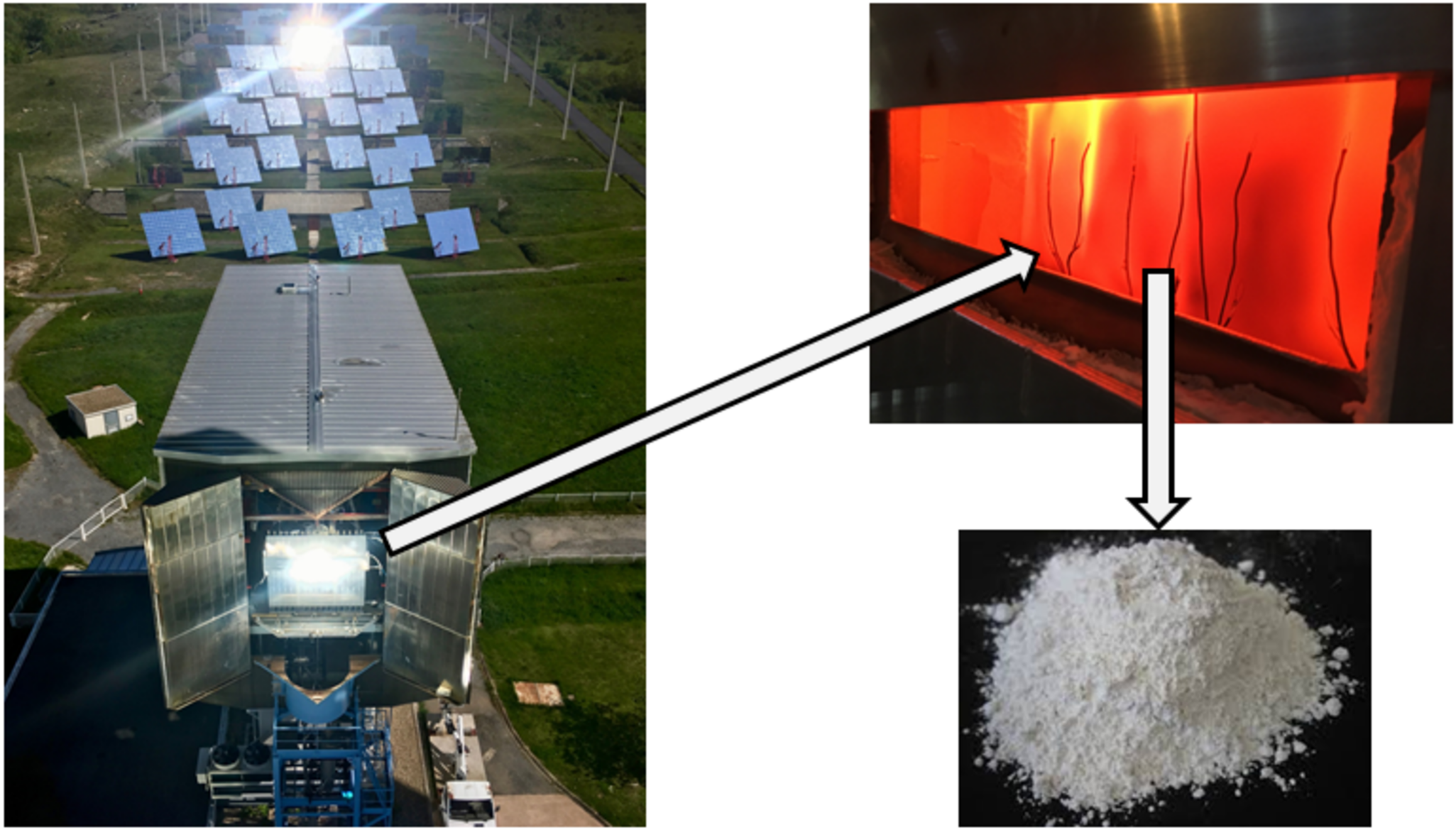
Wen, C.Y., Yu, Y.H., 1966. A Generalized Method for Predicting the Minimum Fluidization Velocity. AIChE Journal 12, 610–612. https://doi.org/10.1002/aic.690120343